

Switchable biexciton in perovskite-like RbCu₂Br₃ crystals driven by thermally induced phase transition

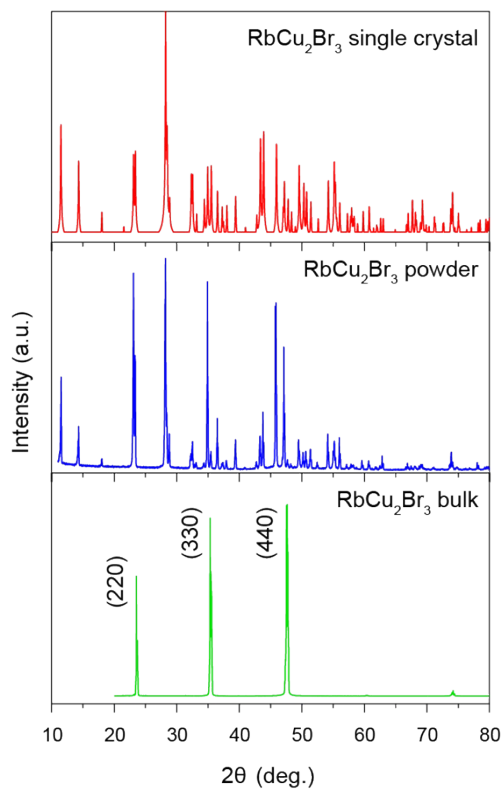
Ying Ding, Richeng Lin, Zhuogeng Lin, Wei Zheng**

State Key Laboratory of Optoelectronic Materials and Technologies, School of
Materials, Sun Yat-sen University, Shenzhen 518107, China

*Correspondence: linrch8@mail.sysu.edu.cn; zhengw37@mail.sysu.edu.cn.

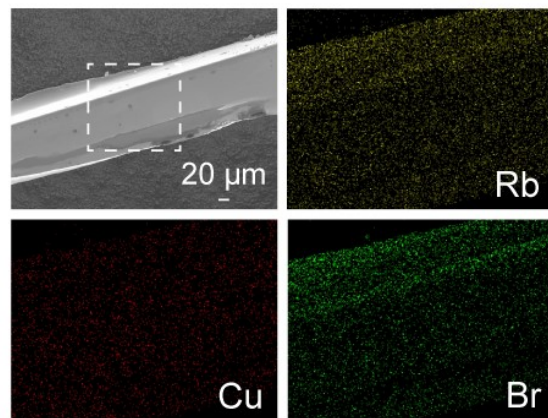
Contents

1. Structural and optical properties of RbCu ₂ Br ₃ crystals.....	2
2. Luminescence transition caused by symmetry breaking in RbCu ₂ Br ₃ crystals	7
3. Direct X-ray detection of RbCu ₂ Br ₃ crystals	11
References	15



1. Structural and optical properties of RbCu₂Br₃ crystals

Figure S1. From top to bottom are the SCXRD patterns, powder XRD patterns, and bulk XRD



patterns of RbCu₂Br₃ crystals.

Figure S2. SEM image of the RbCu₂Br₃ crystal and EDS spectra of elements distribution within the white dashed box.

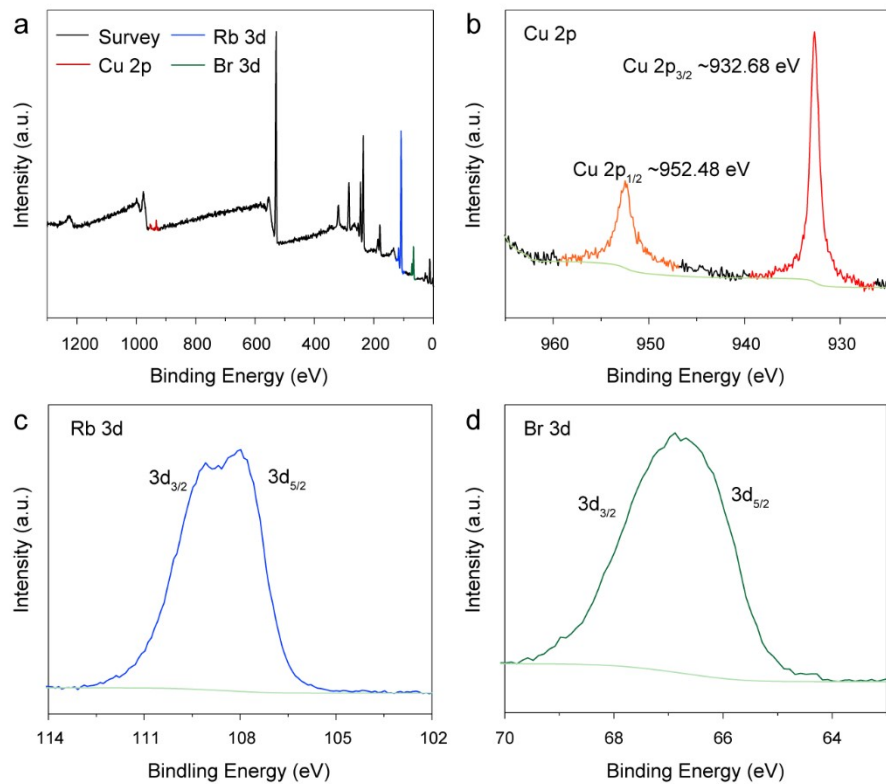
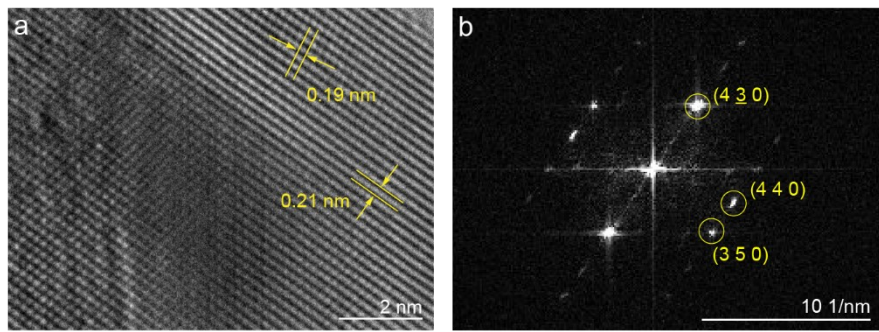
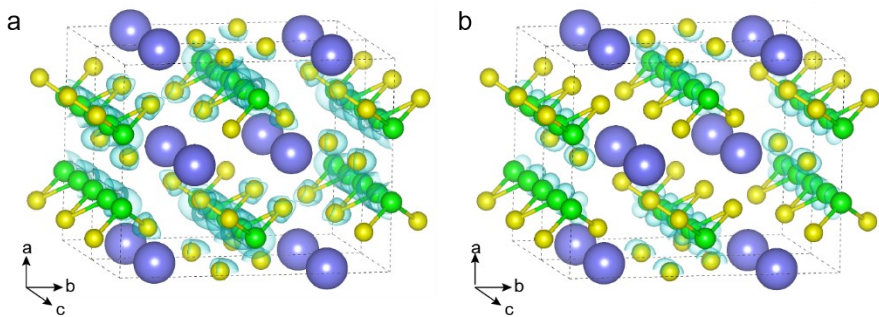


Figure S3. HREM (a) and SAED (b) characterization of RbCu_2Br_3 crystals.

Figure S4. RbCu_2Br_3 crystals XPS full spectrum (a) and core-level spectra amplified in small-scale



energy regions of copper elements (b), rubidium (c) and bromine (d).

Figure S5. Isosurface maps of the real-space charge distribution at the bottom of conduction band

(a) and the top of valence band (b) of the RbCu_2Br_3 .

Table S1. Crystal data and structure refinement for RbCu₂Br₃.

Empirical formula	Rb _{0.5} CuBr _{1.5}
Formula weight	226.14
Temperature	293.15 K
Wavelength	0.71073 Å
Crystal system	Orthorhombic
Space group	C m c m
	a = 9.834(2) Å alpha = 90 deg.
Unit cell dimensions	b = 12.362(3) Å beta = 90 deg.
	c = 5.5333(12) Å gamma = 90 deg.
Volume	672.7(3) Å ³
Z, Calculated density	8, 4.466 g/m ³
Absorption coefficient	31.195 mm ⁻¹
F(000)	800
Crystal size	0.35 x 0.3 x 0.25 mm ³
Theta range for data collection	6.592 to 52.688 deg.
Limiting indices	-12 ≤ h ≤ 11, -15 ≤ k ≤ 14, -6 ≤ l ≤ 6
Reflections collected	863
Independent reflections	397 [R(int) = 0.0430, R(sigma) = 0.0634]
Data / restraints / parameters	397 / 0 / 20
Goodness-of-fit on F ²	1.141
Final R indices [I>2sigma(I)]	R ₁ = 0.0612, wR ₂ = 0.1491
R indices (all data)	R ₁ = 0.0853, wR ₂ = 0.1599
Largest diff. peak and hole	1.60 and -3.19 e/Å ³

Table S2. Fractional atomic coordinates ($\times 10^4$) and equivalent isotropic displacement parameters (Å $^2 \times 10^3$) for RbCu₂Br₃. U_(eq) is defined as one third of the trace of the orthogonalized U_{ij} tensor.

Atom	x	y	z	U _(eq)
Rb(02)	0	8116(3)	7500	38.0(9)
Br(1)	2906(2)	6247.0(17)	7500	36.3(7)
Br(2)	0	3836.7(18)	7500	16.3(7)
Cu(1)	1655(3)	5000	10000	37.5(9)

Table S3. Selected bond lengths [\AA] and angles [deg] for RbCu_2Br_3 .

Br(2)-Rb(02)#1	3.672(2)	Br(1)#9-Rb(02)-Br(2)#1	137.36(7)
Br(2)-Rb(02)#2	3.672(2)	Br(1)#10-Rb(02)-Br(2)#2	63.71(4)
Br(2)-Cu(1)#3	2.575(2)	Br(1)#11-Rb(02)-Br(2)#2	137.36(7)
Br(2)-Cu(1)	2.575(2)	Br(1)#11-Rb(02)-Br(2)#1	63.71(4)
Br(2)-Cu(1)#1	2.575(2)	Br(1)#8-Rb(02)-Br(2)#2	137.36(7)
Br(2)-Cu(1)#4	2.575(2)	Br(1)#10-Rb(02)-Br(1)	126.34(4)
Rb(02)-Br(1)#7	3.675(3)	Br(1)#9-Rb(02)-Br(1)	71.77(5)
Rb(02)-Br(1)#8	3.5379(14)	Br(1)#9-Rb(02)-Br(1)#11	154.28(13)
Rb(02)-Br(1)#9	3.5379(14)	Br(1)#8-Rb(02)-Br(1)	71.77(5)
Rb(02)-Br(1)#10	3.5379(14)	Br(1)#11-Rb(02)-Br(1)#8	71.21(7)
Rb(02)-Br(1)	3.675(3)	Br(1)#10-Rb(02)-Br(1)#8	154.28(13)
Rb(02)-Br(1)#11	3.5379(14)	Br(1)#11-Rb(02)-Br(1)#7	71.77(5)
Br(1)-Cu(1)	2.409(2)	Br(1)#9-Rb(02)-Br(1)#7	126.34(4)
Br(1)-Cu(1)#4	2.409(2)	Br(1)#10-Rb(02)-Br(1)#7	71.77(5)
Rb(02)#1-Br(2)-Rb(02)#2	97.79(9)	Br(1)#11-Rb(02)-Br(1)	126.34(4)
Cu(1)#2-Br(2)-Rb(02)#2	87.84(4)	Br(1)#9-Rb(02)-Br(1)#10	71.21(7)
Cu(1)-Br(2)-Rb(02)#1	140.53(5)	Br(1)#9-Rb(02)-Br(1)#8	102.89(6)
Cu(1)#3-Br(2)-Rb(02)#2	140.53(5)	Br(1)-Rb(02)-Br(1)#7	102.08(10)
Cu(1)-Br(2)-Rb(02)#2	87.84(4)	Br(1)#11-Rb(02)-Br(1)#10	102.89(6)
Cu(1)#3-Br(2)-Rb(02)#1	87.84(4)	Br(1)#8-Rb(02)-Br(1)#7	126.34(4)
Cu(1)#4-Br(2)-Rb(02)#2	140.53(5)	Rb(02)#9-Br(1)-Rb(02)#8	102.89(6)
Cu(1)#4-Br(2)-Rb(02)#1	87.84(4)	Rb(02)#8-Br(1)-Rb(02)	108.23(5)
Cu(1)#2-Br(2)-Rb(02)#1	140.53(5)	Rb(02)#9-Br(1)-Rb(02)	108.23(5)
Cu(1)#3-Br(2)-Cu(1)	64.99(6)	Cu(1)-Br(1)-Rb(02)	90.31(9)
Cu(1)#2-Br(2)-Cu(1)	78.41(10)	Cu(1)#3-Br(1)-Rb(02)#8	89.46(5)
Cu(1)#4-Br(2)-Cu(1)#2	64.99(6)	Cu(1)#3-Br(1)-Rb(02)	90.31(9)
Cu(1)#3-Br(2)-Cu(1)#2	112.10(10)	Cu(1)-Br(1)-Rb(02)#9	89.46(5)
Cu(1)#4-Br(2)-Cu(1)	112.10(10)	Cu(1)-Br(1)-Rb(02)#8	152.72(10)
Cu(1)#3-Br(2)-Cu(1)#4	78.41(10)	Cu(1)#3-Br(1)-Rb(02)#9	152.72(10)
Br(2)#1-Rb(02)-Br(2)#2	97.79(9)	Cu(1)-Br(1)-Cu(1)#3	70.10(7)
Br(2)#2-Rb(02)-Br(1)#7	65.58(5)	Br(2)-Cu(1)-Br(2)#2	101.59(10)
Br(2)#1-Rb(02)-Br(1)#7	65.58(5)	Br(1)#13-Cu(1)-Br(2)#2	111.81(4)
Br(2)#2-Rb(02)-Br(1)	65.58(5)	Br(1)-Cu(1)-Br(2)	111.81(4)
Br(2)#1-Rb(02)-Br(1)	65.58(5)	Br(1)#13-Cu(1)-Br(2)	105.90(7)
Br(1)#8-Rb(02)-Br(2)#1	63.71(4)	Br(1)-Cu(1)-Br(2)#2	105.89(7)
Br(1)#9-Rb(02)-Br(2)#2	63.71(4)	Br(1)#13-Cu(1)-Br(1)	118.60(15)
Br(1)#10-Rb(02)-Br(2)#1	137.36(7)		

Symmetry transformations used to generate equivalent atoms:

#1 -x,1-y,1-z; 2# -x,1-y,2-z; 3# +x,+y,3/2-z; 4# -x,1-y,-1/2+z; 7# -x,+y,3/2-z; 8# 1/2-x,3/2-y,1-z; 9# 1/2-x,3/2-y,2-z; 10# -1/2+x,3/2-y,1/2+z; 11# -1/2+x,3/2-y,-1/2+z; 13# +x,1-y,1/2+z

Table S4. Anisotropic displacement parameters ($\text{\AA}^2 \times 10^3$) for RbCu_2Br_3 . The anisotropic displacement factor exponent takes the form: $-2 \pi^2 [h^2 a^{2*}U_{11} + \dots + 2hk a^*b^*U_{12}]$.

	U11	U22	U33	U23	U13	U12
Rb(02)	35.1(17)	53(2)	26.0(15)	0	0	0
Br(1)	30.7(12)	54.4(15)	23.7(11)	0	0	-31.3(11)
Br(2)	10.5(12)	13.3(12)	25.0(14)	0	0	0
Cu(1)	32.6(15)	42.3(17)	37.6(16)	12.5(12)	0	0

2. Luminescence transition caused by symmetry breaking in RbCu_2Br_3 crystals

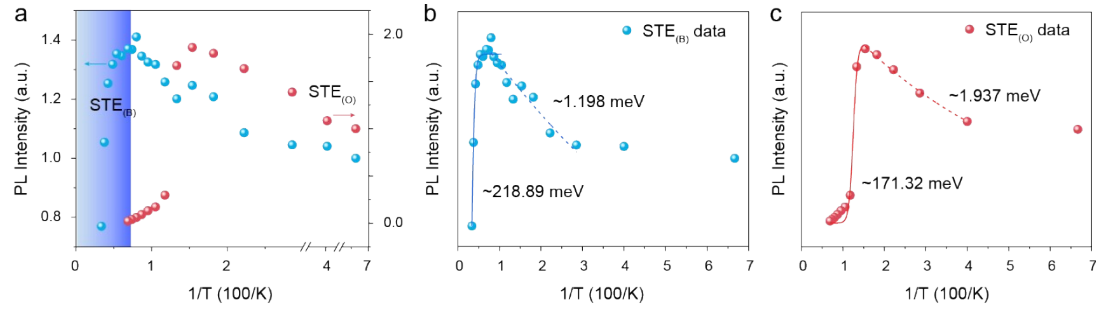


Figure S6. (a) Extraction of temperature-dependent data of the emission peak integral intensity of $\text{STE}_{(\text{B})}$ and $\text{STE}_{(\text{O})}$ in the whole temperature range (8-295 K) of RbCu_2Br_3 crystals. The PL intensities of $\text{STE}_{(\text{B})}$ (b) and $\text{STE}_{(\text{O})}$ (c) are fitted with the change of temperature. The points are experimental data points, and the solid and dotted lines are the fitting curves of formulas (1) and (3), respectively.

Table S5. Crystal data and structure refinement for RbCu₂Br₃ at 100 K.

Empirical formula	RbCu ₂ Br ₃
Formula weight	452.28
Temperature	100.02(10) K
Wavelength	0.71073 Å
Crystal system	Orthorhombic
Space group	P n m a
	a = 12.3099(11) Å alpha = 90 deg.
Unit cell dimensions	b = 5.4479(5) Å beta = 90 deg.
	c = 9.8481(8) Å gamma = 90 deg.
Volume	660.44(10) Å ³
Z, Calculated density	4, 4.549 g/m ³
Absorption coefficient	31.773 mm ⁻¹
F(000)	800
Crystal size	0.14 x 0.13 x 0.12 mm ³
Theta range for data collection	3.904 to 27.494 deg.
Limiting indices	-14 ≤ h ≤ 15, -7 ≤ k ≤ 7, -11 ≤ l ≤ 12
Reflections collected / unique	2442 / 823 [R(int) = 0.0348]
Completeness to theta = 25.242	99.5 %
Absorption correction	Semi-empirical from equivalents
Max. and min. transmission	1.00000 and 0.03601
Refinement method	Full-matrix least-squares on F ²
Data / restraints / parameters	823 / 0 / 34
Goodness-of-fit on F ²	1.068
Final R indices [I > 2sigma(I)]	R ₁ = 0.0347, wR ₂ = 0.0783
R indices (all data)	R ₁ = 0.0408, wR ₂ = 0.0804
Largest diff. peak and hole	1.254 and -1.868 e/Å ³

Table S6. Atomic coordinates ($\times 10^4$) and equivalent isotropic displacement parameters ($\text{\AA}^2 \times 10^3$) for RbCu₂Br₃ at 100 K. U_(eq) is defined as one third of the trace of the orthogonalized U_{ij} tensor.

Atom	x	y	z	U _(eq)
Rb(1)	6898(1)	-2500	208(1)	14(1)
Br(2)	3857(1)	2500	4909(1)	7(1)
Br(1)	6457(1)	2500	2300(1)	10(1)
Br(3)	3941(1)	7500	1851(1)	15(1)
Cu(1)	5048(1)	5006(1)	3328(1)	13(1)

Table S7. Selected bond lengths [\AA] and angles [deg] for RbCu_2Br_3 at 100 K.

Rb(1)-Br(2)#2	3.6396(7)	Br(3)#6-Rb(1)-Br(3)#2	128.469(13)
Rb(1)-Br(2)#3	3.6396(7)	Br(3)#7-Rb(1)-Br(3)#2	128.469(13)
Rb(1)-Br(1)	3.4584(7)	Br(3)#6-Rb(1)-Br(3)#5	88.06(2)
Rb(1)-Br(1)#4	3.5069(11)	Rb(1)#12-Br(2)-Rb(1)#13	96.91(3)
Rb(1)-Br(1)#5	3.4584(7)	Cu(1)-Br(2)-Rb(1)#12	140.01(3)
Rb(1)-Br(3)#6	3.5492(7)	Cu(1)-Br(2)-Rb(1)#13	87.763(19)
Rb(1)-Br(3)#7	3.5492(7)	Cu(1)#9-Br(2)-Rb(1)#13	139.49(3)
Rb(1)-Br(3)#2	3.8359(11)	Cu(1)#8-Br(2)-Rb(1)#12	87.76(2)
Rb(1)-Br(3)#5	3.9835(12)	Cu(1)#10-Br(2)-Rb(1)#13	88.47(2)
Br(2)-Cu(1)	2.5377(8)	Cu(1)#10-Br(2)-Rb(1)#12	139.49(3)
Br(2)-Cu(1)#9	2.5844(9)	Cu(1)#9-Br(2)-Rb(1)#12	88.47(2)
Br(2)-Cu(1)#8	2.5377(8)	Cu(1)#8-Br(2)-Rb(1)#13	140.01(3)
Br(2)-Cu(1)#10	2.5844(9)	Cu(1)#8-Br(2)-Cu(1)#9	80.09(3)
Br(1)-Cu(1)	2.4281(9)	Cu(1)-Br(2)-Cu(1)#8	65.09(3)
Br(1)-Cu(1)#8	2.4280(9)	Cu(1)#8-Br(2)-Cu(1)#10	113.18(3)
Br(3)-Cu(1)#11	2.4125(9)	Cu(1)#10-Br(2)-Cu(1)#9	63.44(3)
Br(3)-Cu(1)	2.4125(9)	Cu(1)-Br(2)-Cu(1)#10	80.09(3)
Br(2)#3-Rb(1)-Br(2)#2	96.91(3)	Cu(1)-Br(2)-Cu(1)#9	113.17(3)
Br(2)#3-Rb(1)-Br(3)#5	128.184(15)	Rb(1)#14-Br(1)-Rb(1)#15	113.324(16)
Br(2)#3-Rb(1)-Br(3)#2	65.766(17)	Rb(1)-Br(1)-Rb(1)#15	113.324(16)
Br(2)#2-Rb(1)-Br(3)#2	65.766(17)	Rb(1)#14-Br(1)-Rb(1)	103.93(3)
Br(2)#2-Rb(1)-Br(3)#5	128.184(15)	Cu(1)#8-Br(1)-Rb(1)#14	143.44(3)
Br(1)#4-Rb(1)-Br(2)#3	65.903(18)	Cu(1)-Br(1)-Rb(1)#15	94.14(3)
Br(1)#5-Rb(1)-Br(2)#3	135.42(3)	Cu(1)#8-Br(1)-Rb(1)	85.27(2)
Br(1)-Rb(1)-Br(2)#3	62.177(16)	Cu(1)#8-Br(1)-Rb(1)#15	94.14(3)
Br(1)-Rb(1)-Br(2)#2	135.42(3)	Cu(1)-Br(1)-Rb(1)#14	85.27(2)
Br(1)#5-Rb(1)-Br(2)#2	62.177(16)	Cu(1)-Br(1)-Rb(1)	143.44(3)
Br(1)#4-Rb(1)-Br(2)#2	65.903(18)	Cu(1)#8-Br(1)-Cu(1)	68.42(4)
Br(1)-Rb(1)-Br(1)#4	125.244(14)	Rb(1)#7-Br(3)-Rb(1)#14	91.94(2)
Br(1)-Rb(1)-Br(1)#5	103.93(3)	Rb(1)#13-Br(3)-Rb(1)#14	154.93(3)
Br(1)#5-Rb(1)-Br(1)#4	125.244(14)	Rb(1)#6-Br(3)-Rb(1)#14	91.94(2)
Br(1)#5-Rb(1)-Br(3)#5	67.334(17)	Rb(1)#6-Br(3)-Rb(1)#13	103.924(18)
Br(1)#5-Rb(1)-Br(3)#2	69.690(18)	Rb(1)#7-Br(3)-Rb(1)#6	100.26(3)
Br(1)-Rb(1)-Br(3)#6	71.957(16)	Rb(1)#7-Br(3)-Rb(1)#13	103.924(18)
Br(1)#4-Rb(1)-Br(3)#5	149.23(3)	Cu(1)-Br(3)-Rb(1)#7	94.391(19)
Br(1)#4-Rb(1)-Br(3)#7	72.63(2)	Cu(1)#11-Br(3)-Rb(1)#7	160.23(3)

Br(1)#4-Rb(1)-Br(3)#6	72.63(2)	Cu(1)-Br(3)-Rb(1)#14	74.25(3)
Br(1)#5-Rb(1)-Br(3)#6	154.06(3)	Cu(1)#11-Br(3)-Rb(1)#13	85.14(3)
Br(1)#5-Rb(1)-Br(3)#7	71.958(16)	Cu(1)#11-Br(3)-Rb(1)#14	74.25(3)
Br(1)#4-Rb(1)-Br(3)#2	103.77(3)	Cu(1)-Br(3)-Rb(1)#6	160.23(3)
Br(1)-Rb(1)-Br(3)#2	69.691(18)	Cu(1)-Br(3)-Rb(1)#13	85.14(3)
Br(1)-Rb(1)-Br(3)#5	67.334(17)	Cu(1)#11-Br(3)-Rb(1)#6	94.390(19)
Br(1)-Rb(1)-Br(3)#7	154.06(3)	Cu(1)#11-Br(3)-Cu(1)	68.56(4)
Br(3)#6-Rb(1)-Br(2)#3	66.439(17)	Br(2)-Cu(1)-Br(2)#10	99.91(3)
Br(3)#6-Rb(1)-Br(2)#2	138.51(3)	Br(1)-Cu(1)-Br(2)#10	101.71(3)
Br(3)#7-Rb(1)-Br(2)#2	66.439(17)	Br(1)-Cu(1)-Br(2)	111.48(3)
Br(3)#7-Rb(1)-Br(2)#3	138.51(3)	Br(3)-Cu(1)-Br(2)	110.26(3)
Br(3)#2-Rb(1)-Br(3)#5	107.001(19)	Br(3)-Cu(1)-Br(2)#10	113.81(3)
Br(3)#7-Rb(1)-Br(3)#5	88.06(2)	Br(3)-Cu(1)-Br(1)	117.97(4)
Br(3)#7-Rb(1)-Br(3)#6	100.26(3)		

Symmetry transformations used to generate equivalent atoms:

#2 x+1/2,y-1,-z+1/2 #3 x+1/2,y,-z+1/2 #4 -x+3/2,-y,z-1/2 #5 x,y-1,z #6 -x+1,-y+1,-z
#7 -x+1,-y,-z #8 x,-y+1/2,z #9 -x+1,y-1/2,-z+1 #10 -x+1,-y+1,-z+1 #11 x,-y+3/2,z
#12 x-1/2,y,-z+1/2 #13 x-1/2,y+1,-z+1/2 #14 x,y+1,z #15 -x+3/2,-y,z+1/2

Table S8. Anisotropic displacement parameters ($\text{\AA}^2 \times 10^3$) for RbCu₂Br₃ at 100 K. The anisotropic displacement factor exponent takes the form: $-2 \pi^2 [h^2 a^{2*}U_{11} + \dots + 2hk a^*b^*U_{12}]$.

	U11	U22	U33	U23	U13	U12
Rb(1)	14(1)	10(1)	18(1)	0	3(1)	0
Br(2)	1(1)	10(1)	11(1)	0	0(1)	0
Br(1)	7(1)	10(1)	15(1)	0	5(1)	0
Br(3)	16(1)	10(1)	20(1)	0	-11(1)	0
Cu(1)	9(1)	12(1)	19(1)	2(1)	1(1)	4(1)

3. Direct X-ray detection of RbCu₂Br₃ crystals

The ability of an X-ray detector to collect charges can be measured by the product of carrier mobility μ and charge carrier lifetime τ , that is, a larger $\mu\tau$ means a stronger ability. The photoconductivity is fitted using the modified Hecht equation as follows ^{1, 2}:

$$I = \frac{I_0 \mu \tau V^{1 - \exp(-\frac{L^2}{\mu \tau V})}}{L^2 + \frac{Ls}{V\mu}}$$

where I_0 , V , L and s respectively refer to saturated photocurrent, applied voltage, device thickness and surface recombination velocity. As shown in **Figure S9**, the fitting result of $\mu\tau$ is $6.586 \times 10^{-5} \text{ cm}^2 \text{ V}^{-1}$, which is comparable to that of other single-crystal perovskites such as (PEA)₂PbBr₄ ($4.4 \times 10^{-4} \text{ cm}^2 \text{ V}^{-1}$), Cs₃Bi₂I₉ ($2.03 \times 10^{-5} \text{ cm}^2 \text{ V}^{-1}$), Rb₃Bi₂I₉ ($1.7 \times 10^{-6} \text{ cm}^2 \text{ V}^{-1}$)³⁻⁶. It is two orders of magnitude higher than the current mature commercial a-Se ($10^{-7} \text{ cm}^2 \text{ V}^{-1}$)⁷.

The sensitivity (S) of X-ray detector is a key indicator to reflect the ability to identify changes in X-ray metering. Through the photocurrent response under different electric fields and with different X-ray doses (**Figure S10a**), the

detector sensitivity can be obtained through the formula of $S = \frac{I_{ph}}{DA}$ (the photocurrent $I_{ph} = I_{light} - I_{dark}$; D is the X-ray irradiation dose rate; A is the effective irradiation area of the detector)⁸, as shown in **Figure S10b**. With a field strength of 20 V mm^{-1} , the sensitivity of this detector reaches $29.3 \mu\text{C Gy}_{\text{air}}^{-1} \text{ cm}^{-2}$, which is comparable to that of stabilized a-Se detector ($20 \mu\text{C Gy}_{\text{air}}^{-1} \text{ cm}^{-2}$) with a working field strength of 10^4 V mm^{-1} ⁹. And the sensitivity is similar to that of mature halide crystals (e.g. Cs₂TeI₆ $27.8 \mu\text{C Gy}_{\text{air}}^{-1} \text{ cm}^{-2}$; MAPbBr₃ $80 \mu\text{C Gy}_{\text{air}}^{-1} \text{ cm}^{-2}$; Cs₂AgBiBr₆ $105 \mu\text{C Gy}_{\text{air}}^{-1} \text{ cm}^{-2}$), meeting the needs of X-ray detection¹⁰⁻¹². In addition, according to the International Union of Pure and Applied Chemistry (IUPAC), only when the signal-to-noise ratio (SNR) is greater than 3 can the obtained signal be considered as identifiable. **Figure S11** is the I-T curve

of applied electric field of 20 V mm^{-1} with different radiation doses. Based on the formula of $\text{SNR} = I_{\text{signal}} / I_{\text{noise}}$ (I_{signal} is the signal current obtained by subtracting the average dark current from the average photocurrent, and I_{noise} is the noise current equal to the standard deviation of photocurrent), under the bias voltage of 20 V mm^{-1} , the detection limit of this RbCu_2Br_3 detector is about $1.41 \mu\text{Gy}_{\text{air}} \text{ s}^{-1}$, which is much lower than the standard $5.5 \mu\text{Gy}_{\text{air}} \text{ s}^{-1}$ for routine medical diagnosis⁸.

The stability is another important indicator for X-ray detectors. **Figure S12a** shows the I-T curves in different applied electric fields with a radiation dose of $9.74 \mu\text{Gy}_{\text{air}} \text{ s}^{-1}$. It can be observed that this detector exhibits repeatable optoelectronic properties in the case of periodic ray response. The rising and falling edges of each individual X-ray response are extracted (**Figure S12b,c**), where the rise (fall) time is defined as the time it takes for the photocurrent to rise (fall) to 90% (10%) of its maximum value. As bias voltage increases, the switching time remains in a range, indicating that the effect of applied electric field on the carrier transport inside this detector almost can be ignored.

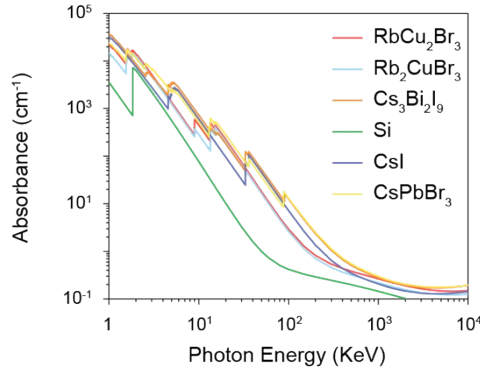


Figure S7. The diagram of absorption coefficients corresponding to photon energy of RbCu_2Br_3 crystals and common scintillators.

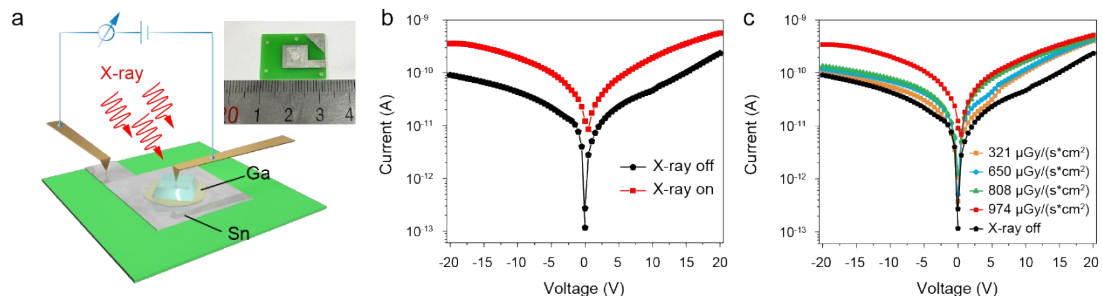


Figure S8. RbCu_2Br_3 crystals are used in the study of direct X-ray detection. (a) The RbCu_2Br_3 crystals-based vertical detector ($\text{Au}/\text{RbCu}_2\text{Br}_3/\text{Ga}/\text{Sn}$) prepared in this work with the physical image shown in the inset. (b) I-V curve of the detector in the on/off state of X-ray. (c) I-V curves of this detector with different X-ray doses.

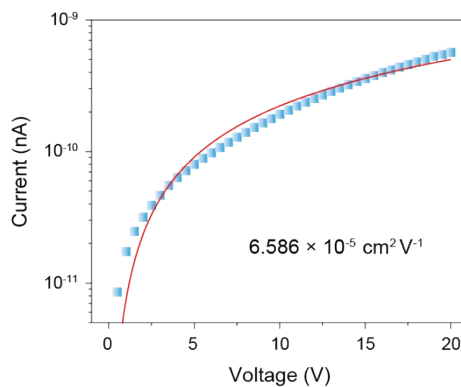


Figure S9. Bias-dependent photoconductivity of the RbCu_2Br_3 -based vertical device under X-ray excitation. The points are experimental data, and the curve is the fitting curve of the Hecht equation.

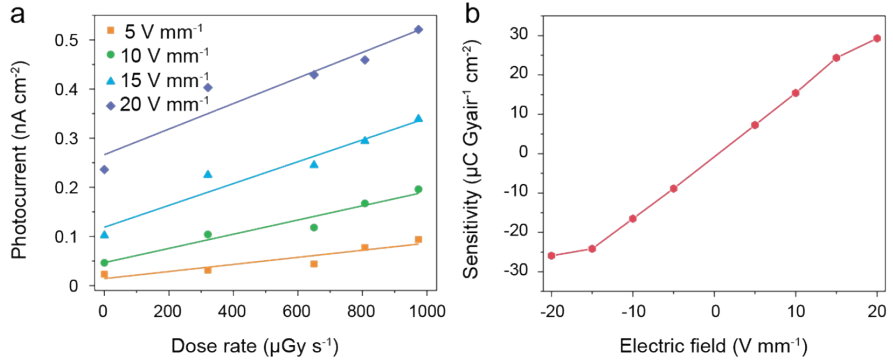


Figure S10. Photocurrent responses of RbCu_2Br_3 with different X-ray doses and electric fields (a), and the sensitivity of this detector in different applied electric fields (b).

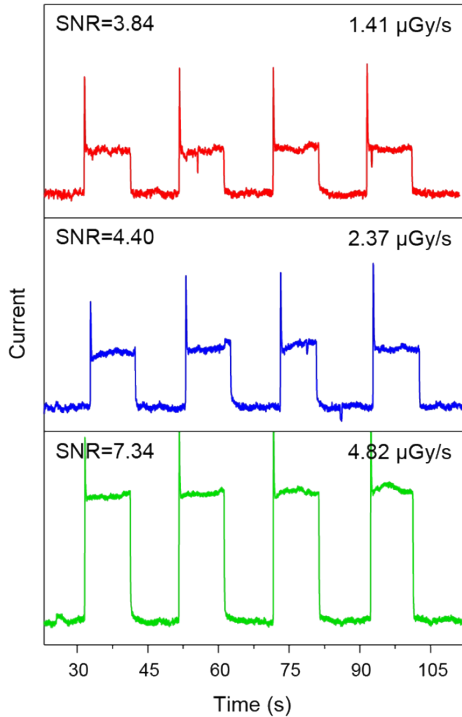


Figure S11. The I-T curves of the RbCu_2Br_3 -based detector under 20 V mm^{-1} electric field with different X-ray doses. Corresponding SNRs have been calculated.

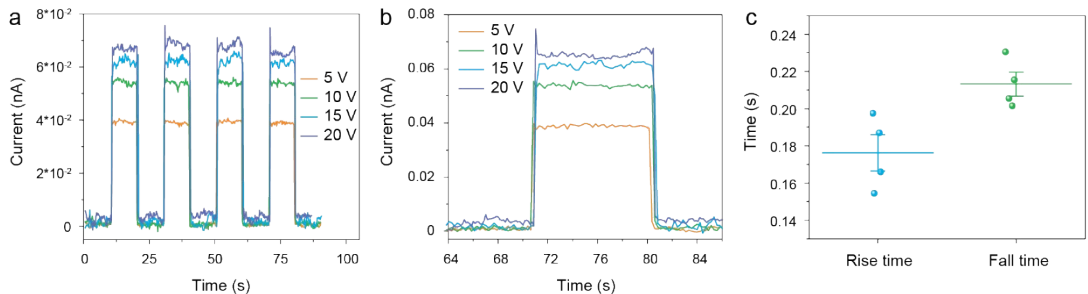


Figure S12. Time response of RbCu_2Br_3 -based detector. (a) I-T curves of 9.74 $\mu\text{Gy air s}^{-1}$ radiation dose in different applied electric fields. (b), (c) Switching time obtained by extracting the rising and falling edges of a single ray response.

References

1. Q. Dong, Y. Fang, Y. Shao, P. Mulligan, J. Qiu, L. Cao and J. Huang, Electron-hole diffusion lengths > 175 mm in solution-grown CH₃NH₃PbI₃ single crystals, *Science*, 2015, **347**, 967-970.
2. C. C. Stoumpos, C. D. Malliakas, J. A. Peters, Z. Liu, M. Sebastian, J. Im, T. C. Chasapis, A. C. Wibowo, D. Y. Chung, A. J. Freeman, B. W. Wessels and M. G. Kanatzidis, Crystal Growth of the Perovskite Semiconductor CsPbBr₃: A New Material for High-Energy Radiation Detection, *Cryst. Growth Des.*, 2013, **13**, 2722-2727.
3. Y. Zhang, Y. Liu, Z. Xu, H. Ye, Q. Li, M. Hu, Z. Yang and S. Liu, Two-dimensional (PEA)₂PbBr₄ perovskite single crystals for a high performance UV-detector, *Journal of Materials Chemistry C*, 2019, **7**, 1584-1591.
4. S. Deumel, A. van Breemen, G. Gelinck, B. Peeters, J. Maas, R. Verbeek, S. Shanmugam, H. Akkerman, E. Meulenkamp, J. E. Huerdler, M. Acharya, M. García-Batlle, O. Almora, A. Guerrero, G. García-Belmonte, W. Heiss, O. Schmidt and S. F. Tedde, High-sensitivity high-resolution X-ray imaging with soft-sintered metal halide perovskites, *Nat. Electron.*, 2021, **4**, 681-688.
5. K. M. McCall, Z. Liu, G. Trimarchi, C. C. Stoumpos, W. Lin, Y. He, I. Hadar, M. G. Kanatzidis and B. W. Wessels, α -Particle Detection and Charge Transport Characteristics in the A₃M₂I₉ Defect Perovskites (A = Cs, Rb; M = Bi, Sb), *ACS Photonics*, 2018, **5**, 3748-3762.
6. Q. Sun, Y. Xu, H. Zhang, B. Xiao, X. Liu, J. Dong, Y. Cheng, B. Zhang, W. Jie and M. G. Kanatzidis, Optical and electronic anisotropies in perovskitoid crystals of Cs₃Bi₂I₉ studies of nuclear radiation detection, *J. Mater. Chem. A*, 2018, **6**, 23388-23395.
7. S. O. Kasap, X-ray sensitivity of photoconductors: application to stabilized a-Se, *J. Phys. D: Appl. Phys.*, 2000, **33**, 2853–2865.
8. Y. Zhang, Y. Liu, Z. Xu, H. Ye, Z. Yang, J. You, M. Liu, Y. He, M. G. Kanatzidis and S. F. Liu, Nucleation-controlled growth of superior lead-free perovskite Cs₃Bi₂I₉ single-crystals for high-performance X-ray detection, *Nat. Commun.*, 2020, **11**, 2304.
9. M. C. B. Polischuk, *Direct selenium x-ray detector for fluoroscopy, R&F, and radiography*,

- Proc. SPIE, 2000.
10. B. Xiao, F. Wang, M. Xu, X. Liu, Q. Sun, B.-B. Zhang, W. Jie, P. Sellin and Y. Xu, Melt-grown large-sized Cs₂TeI₆ crystals for X-ray detection, *CrystEngComm*, 2020, **22**, 5130-5136.
 11. W. Pan, H. Wu, J. Luo, Z. Deng, C. Ge, C. Chen, X. Jiang, W.-J. Yin, G. Niu, L. Zhu, L. Yin, Y. Zhou, Q. Xie, X. Ke, M. Sui and J. Tang, Cs₂AgBiBr₆ single-crystal X-ray detectors with a low detection limit, *Nature Photon.*, 2017, **11**, 726-732.
 12. H. Wei, Y. Fang, P. Mulligan, W. Chuirazzi, H.-H. Fang, C. Wang, B. R. Ecker, Y. Gao, M. A. Loi, L. Cao and J. Huang, Sensitive X-ray detectors made of methylammonium lead tribromide perovskite single crystals, *Nature Photon.*, 2016, **10**, 333-339.